Nanoscale

Dynamic Article Links

Cite this: *Nanoscale*, 2012, **4**, 1824

www.rsc.org/nanoscale

REVIEW

Graphene: nanoscale processing and recent applications

László P. Biró,*[a] Péter Nemes-Incze[a] and Philippe Lambin[b]

Received 10th August 2011, Accepted 10th October 2011
DOI: 10.1039/c1nr11067e

One of the most interesting features of graphene is the rich physics set up by the various nanostructures it may adopt. The planar structure of graphene makes this material ideal for patterning at the nanoscale. The breathtakingly fast evolution of research on graphene growth and preparation methods has made possible the preparation of samples with arbitrary sizes. Available sample production techniques, combined with the right patterning tools, can be used to tailor the graphene sheet into functional nanostructures, even whole electronic circuits. This paper is a review of the existing graphene patterning techniques and potential applications of related lithographic methods.

1. Introduction

Due to its many extraordinary properties,[1] graphene, the first truly single-atom thick material,[2] a honeycomb network of sp^2 carbon atoms, is in a winning position for the title of wonder material of the 21st century. Treated as a hypothetical material, its electronic properties were already studied in 1947 by Wallace,[3] whose results were used during the past two decades to describe the electronic properties of single-walled carbon nanotubes. Despite the introduction of the definition for graphene into IUPAC terminology in 1994,[4] it took another 10 years until this unusual material was made widely accessible by the ingenious micromechanical cleavage method[2] and by the visualization of a single-atom thick layer by a common optical microscope.[5] Soon after, an explosive development was started in the field of graphene research, which continues to this day (see Fig. 1). As one can see, the availability of graphene samples and its remarkable properties, promising an extremely wide range of applications,[1] are responsible for an increase of the number of graphene-related papers by a factor of about forty in seven years (from 2004).

It is beyond the scope of the present review to try to list the full range of possible applications of graphene. It is important to cite a few promising ones: high-frequency analog circuits,[8] spintronics,[9] nanoelectronics,[10–12] chemical and biological

[a]*Research Institute for Technical Physics and Materials Science, H-1525 Budapest, P.O. Box 49, Hungary. Web: http://www.nanotechnology.hu/; E-mail: biro@mfa.kfki.hu*
[b]*Facultés Universitaires Notre-Dame de la Paix, 61 Rue de Bruxelles, B-5000 Namur, Belgium*

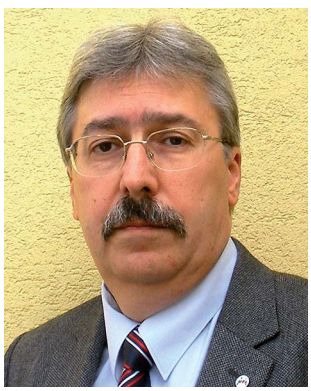

László P. Biró

László Péter Biró is the founding head of the Nanostructures Department in the Research Institute for Technical Physics and Materials Science of the Hungarian Academy of Sciences. He received his PhD degree in 1997 from the Technical University of Budapest after contributing to STM and AFM investigation of surface nanostructures produced by ion irradiation. In 2005, he became a Doctor of the Hungarian Academy of Sciences for his work on carbon nanotube-type nanostructures. Currently, he is interested in the nanolithography of graphene and graphene type materials and in photonic nanoarchitectures of biological origin and bioinspiration.

Péter Nemes-Incze

Péter Nemes-Incze is a PhD student at the Nanostructures Department in the Research Institute for Technical Physics and Materials Science of the Hungarian Academy of Sciences and the Eötvös Lóránd University. Among his research interests is the preparation and scanning probe microscopy characterization of graphene nanostructures. In 2010 he has won the most prestigious scientific prize in Hungary for young researchers, the Junior Prima Prize, for his work on graphene nanolithography.

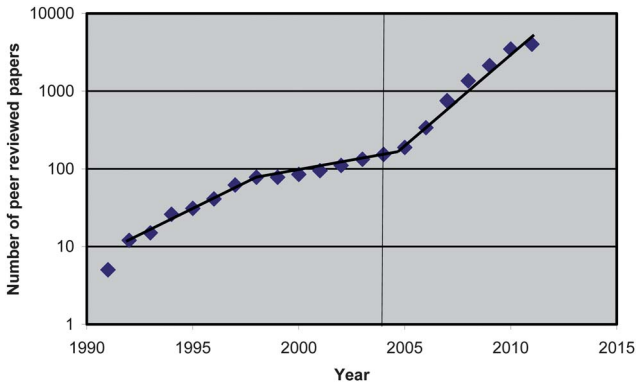

Fig. 1 Number of graphene-related papers according to the Web of Science database. The data for 2011 are extrapolated by doubling the number of publications found in the database as on 14 June 2011. The vertical line marks the year 2004, when Geim and Novoselov published the mechanical cleavage method.[2] It is important to point out, however, that a few of the most important properties of the graphene monolayer were determined experimentally well before the year 2004, including the plasmon structure[6] and the phonon dispersion branches.[7]

sensing,[13–15] composites,[16] gene sequencing,[17] energy storage,[18] *etc.* While many of these applications do not require a precise nanoscale processing of the single atom thick sheet, there are numerous very exciting applications such as digital nanoelectronics and spintronics for which the precise engineering of graphene nanoribbons (GNRs)[19–21] or antidot lattices[22,23] is mandatory. This is an extremely challenging task as the properties of GNRs and of other graphene nanoarchitectures depend strongly on both the crystallographic orientation of their edges and the width of the GNR,[24,25] and the actual atomic structure of the edges,[26,27] including edge disorder which also has important effects on the properties of the graphene nanodevices.[27–29] To date, only few nanoprocessing methods[19,30,31] have been reported, which can meet the very strict criteria for nanopatterning of graphene, namely, crystallographic orientation control and atomic scale precision.

Philippe Lambin

Philippe Lambin is a specialist in theoretical physics of the condensed matter and, more recently, of nanomaterials. He graduated in physical engineering from the University of Liège (BE) in 1976 and obtained his PhD in physical sciences in 1981. After having joined the University of Namur (BE), he went to the IBM Research Center of San Jose (CA) as visiting scientist (1983–1984). Back to Namur as research associate of the Foundation for Scientific Research of Belgium, he became professor in 1995 and full professor in 2004. He was successively dean of the faculty of sciences (2005–2008) and vice-rector of the University of Namur (2008–2011).

2. Graphene: atomic and electronic structure

Carbon is an extremely versatile element, not only in the form of organic compounds, but also in inorganic (nano)materials. The two well-known allotropes of crystalline carbon, graphite with sp^2 hybridization (black, good electric conductor, soft) and diamond with sp^3 hybridization (transparent, insulator, hard), have very different physical properties. The large variety of sp^2 nanocarbons (Fig. 1 in ref. 32)—some of them being well documented, while others are still hypothetical—obtained by various ways of stacking graphitic elements and/or by incorporating defects in the graphitic network have an even wider range of physical properties depending on their particular structure or, in other words, on the way their constituting atoms are linked together. For example, the incorporation of non-hexagonal rings in the honeycomb network transforms straight carbon nanotubes into helical coils.[33–35] To a certain degree, graphene can be regarded as the building block of all these sp^2 nanocarbons.

The flat, perfect and infinite hexagonal network of carbon atoms has special physical properties. The six atoms located at the apexes of the hexagons form two sublattices, A and B. An A atom cannot occupy the position of a B atom without breaking the lattice symmetry (see Fig. 2). This fact has profound implications on the electronic structure of graphene.[2]

The carbon atoms in the two sublattices of graphene form trigonal σ bonds with each other, with an interatomic nearest neighbor separation of $a_{cc} = 1.42$ Å (see Fig. 3). The σ bonding sp^2 orbitals are formed by the superposition of the s, p_x and p_y orbitals of the atomic carbon, leaving the p_z orbital unhybridized. The geometry of the hybridized orbitals is trigonal planar.

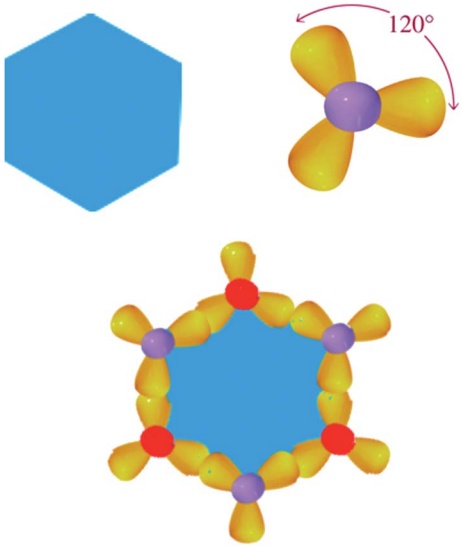

Fig. 2 Construction of the graphene lattice. The hexagonal unit cell is made up of sp^2 hybridized carbon atoms (in top view) to generate a graphitic, honeycomb network. One may observe that the six carbon atoms make up two families—the purple (A) and red (B) positions—which can replace each other by simple translations, while no red atom can replace a purple atom only by a translation operation.

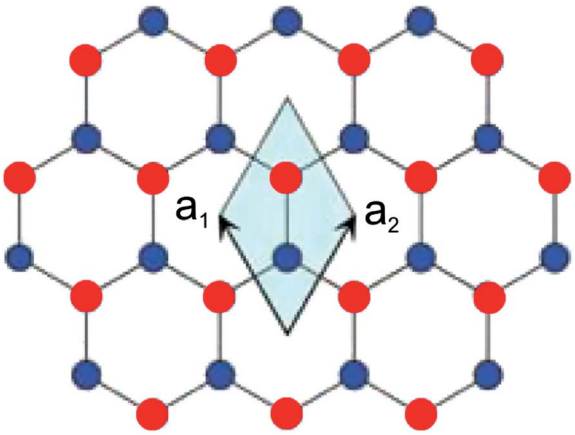

Fig. 3 The honeycomb lattice of graphene. The unit cell defined by vectors a_1 and a_2 containing the two atoms belonging to sublattices A (blue) and B (red) is highlighted in light blue.

This is the reason why each carbon atom has three nearest neighbors within the graphene sheets. Each p_z orbital overlaps with those of the neighboring carbon atoms to form π-bonds that lead to delocalized electron π bands, much like in the case of benzene, naphthalene, anthracene and other aromatic molecules. In this regard, graphene can be thought of as the extreme size limit of planar aromatic molecules. The covalent σ bonds (shorter than the C–C bonds in diamond) are largely responsible for the mechanical strength of graphene and other sp^2 carbon allotropes. The occupied σ electronic bands are completely filled and have a large separation in energy from the Fermi level. For that reason, their effects on the electronic properties of graphene can be neglected, at least to a first approximation. At this level of approximation, the band structure—and therefore the electronic properties—of graphene can be addressed by describing the π bands in a tight binding approximation.[3]

Band structure calculations[3,36] for the honeycomb lattice shown in Fig. 3 yield an unusual electronic structure: the conduction π band and the valence π band of graphene meet exactly at the corners of the hexagonal first Brillouin zone (Fig. 4) and only there. These corners are called the Dirac points. Three of them, labeled as K, belong to one triangular sublattice in reciprocal space, while the other three, labeled as K′, form the second sublattice. The valence and conduction bands meet at the K and K′ points, but do not overlap, with zero number of states just at these points. Because of this, graphene is called a zero band-gap semiconductor or semimetal. Around the Dirac points, the dispersion relation of the π bands is linear with the separation distance, opposite to the other semiconductors, which chiefly exhibit a parabolic dispersion at the Fermi energy. This linear dispersion is at the origin of the unusual electronic properties of graphene.

A linear dispersion normally characterizes particles whose kinetic energy is much larger than their rest mass energy, the best example of which being photons. Thus, electrons in graphene mimic the behavior of photons or other ultra-relativistic particles, with an energy-independent Fermi velocity (v_F) that is approximately 300 times smaller than the speed of light. The energy around the K points can be written as $E = \hbar v_F|\vec{k}|$, where $\vec{k}$ is the wave vector. This linear $E(k)$ dependence is a hallmark of graphene and is in sharp contrast with the behavior of electrons near the band edges in most semiconductors, which if expressed in the effective-mass approximation yields a quadratic relationship: $E(k) \approx \hbar^2k^2/2m_{\text{eff}}$, where m_{eff} stands for the effective mass.

The Hamiltonian describing the electrons and holes near the K, K′ points in graphene may be written as $H = v_F\vec{\sigma}\vec{p}$, where $\vec{p} = \hbar\vec{k}$ and σ are Pauli spin matrices acting on the two honeycomb sublattice degrees of freedom.[37] This is the Dirac equation for massless relativistic particles. The positive energy conduction band and the negative energy valence band touch at the K points, just as electron and positron bands touch at zero momentum in the zero mass limit of the relativistic Dirac equation. This is the reason why the first Brillouin-zone corners in graphene are often referred to as Dirac points.[38]

The existence of two sublattices A and B (corresponding to the two atoms per unit cell) leads to the existence of a novel property of the charge carriers in graphene, where the two linear branches of graphene energy dispersion (intersecting at Dirac points) become independent of each other, indicating the existence of a pseudospin quantum number analogous to electron spin (but completely independent of real spin). Thus, charge carriers in graphene have a pseudospin index in addition to the spin index. The existence of the chiral pseudospin quantum number is a natural product of the basic lattice structure of graphene.[39]

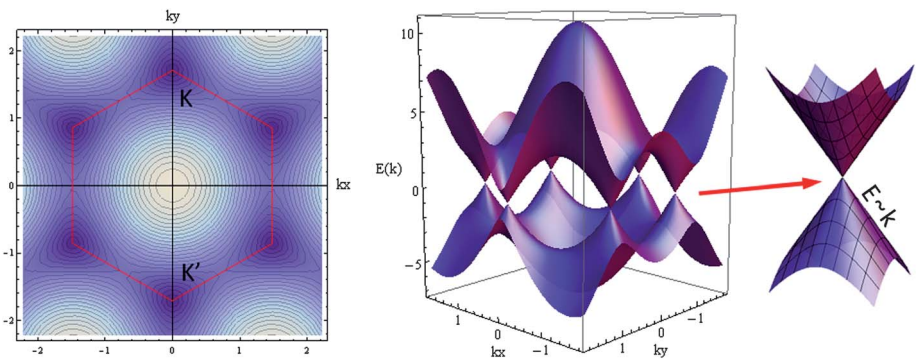

Fig. 4 Contour plot of the energy in the first Brillouin zone of graphene (red hexagon). Plot of the π band structure of graphene, showing the conduction band and the valence band touching at the K points. The zoomed part at the right-hand side shows the linear dispersion in the region of the Dirac points.

This Dirac physics of the charge carriers is the root cause of a lot of interesting physics observed in graphene (for a review, see ref. 36). A good example of this Dirac fermion behavior is the observation of an anomalous, so-called half integer, quantum Hall effect in graphene,[40] where the sequence of steps in the Hall conductivity is shifted by half with respect to the normal quantum Hall effect. Another consequence of the gapless linear bands of graphene is the peculiar scattering properties of its charge carriers, which can have a transmission probability of unity[41] for certain incidence angles upon an electrostatic potential barrier. This phenomenon, known as Klein tunneling, is present both in single-layer and bilayer graphene, although with different intensity and at different incidence angles of the charge carriers upon the potential barrier. For example, a circular, bilayer n–p junction (NPJ) of graphene is predicted to lack the electron beam focusing effect found in a monolayer circular NPJ.[42] The Klein tunneling means that charge carriers in graphene cannot be confined by electrostatic potentials in a similar way as in semiconductors. Therefore, in order to confine charge carriers, one has to produce a discontinuity in the graphene lattice. This raises questions relating to the edge structure of graphene nanoarchitectures with finite dimensions. The simplest of these nanoarchitectures are the so-called GNRs, rectangular strips of a few nanometres in width and having a length significantly larger than their width. One can distinguish three different cases for the edge termination of such GNRs: (i) zigzag (z-GNR) termination; (ii) armchair (a-GNR) termination; (iii) an edge termination associated with any other angle chosen between armchair and zigzag directions (see Fig. 5 for the definition of a-GNRs and z-GNRs).

The a-GNRs are particularly interesting because, for a small enough width and precise crystallographic orientation of their edges, they may exhibit semiconductor behavior with a confinement-induced band gap, large enough to allow the room temperature operation of nanoelectronic devices.[20,25] In contrast with a-GNRs, the z-GNRs are metallic[43] so that they may play the same role as interconnects in Si-based integrated circuits (ICs) or in future all-carbon ICs.[10] Precise zigzag termination of graphene nanoarchitectures was important for the experimental confirmation of theoretical predictions concerning the differences in the Raman signature of armchair and zigzag terminated edges,[30] furthermore spintronic applications[44] of such nanoarchitectures are foreseen. However, under certain conditions the zigzag termination may turn out to be unstable with respect to a planar reconstruction of the edge, which influences the electronic structure of the ribbon.[45]

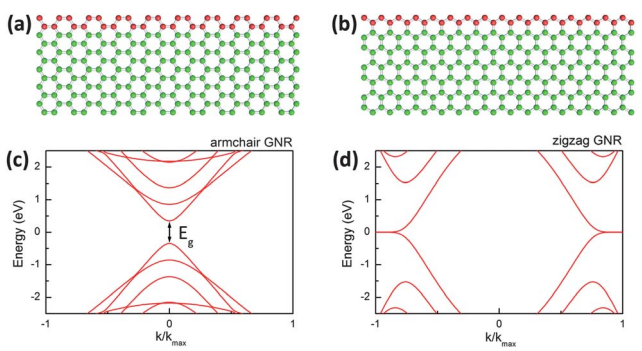

Fig. 5 (a and b) The edge structure of z-GNRs and a-GNRs. (c and d) Schematic band structure in the region of the K points of z-GNR and a-GNR. The a-GNR exhibits a band gap E_g inversely proportional to its width.

The reason for the very different properties of the a-GNRs as compared with the z-GNRs finds its root in the partition of the honeycomb lattice into two sublattices: A and B. A zigzag edge contains carbon atoms from only one sublattice (A or B), while the armchair edge contains atoms from both sublattices A and B. A random edge (oriented under a randomly chosen angle between armchair and zigzag orientations) can be regarded as being composed of armchair and zigzag portions; its electronic properties will be close to those of a zigzag edge.[43,46] This finding may explain why it was impossible to evidence orientation dependence in the behavior of GNRs produced by e-beam lithography.[47] Other theoretical models predict semiconductor-like behavior due to spontaneous rearrangement of defects at z-GNR edges[48] or more complex effects at both zigzag edges and armchair edges, which may produce profound modifications depending on the kind of disorder and the dimensions of the GNR.[27]

3. Top down nanostructuring

3.1. Electron-beam lithography

The usual method for the production of 2D patterns on the scale of 10–100 nm is e-beam lithography followed by plasma etching. Several groups have used this technique for the experimental realization of the first GNRs,[47,49] single electron transistors (SETs)[50] and field effect transistors (FETs).[51]

In order to open a practically relevant band gap in nanostructured graphene, it must be nanopatterned to critical dimensions smaller than 20 nm. However, 20 nm is on the threshold of what can easily be achieved using conventional electron beam lithography due to known electron scattering effects in common electron beam resists.[52] Features down to 10 nm have recently been demonstrated in the production of high-density magnetic media[53] thanks to an experimental resist system. However, according to both theoretical predictions[25] and experimental data,[47] nanopatterned GNRs would present a gap value of the order of 100 meV if their width could be reduced to 10 nm. A gap of this magnitude clearly excludes room temperature operation of the nanodevices. Additionally e-beam lithography does not allow the control of the crystallographic orientation of the GNRs in a straightforward way, which is a crucial factor in obtaining a suitably large band gap.[25]

An eloquent illustration of a problem that may arise due to the limitations of the e-beam lithography is provided by ref. 54 (see Fig. 6.). Two distinct voltage scales were found to characterize the parameter region of suppressed conductance at low charge density in the ribbon. One of them is related to the charging energy of localized states and the other to the strength of the disorder potential. The transport gap in an etched GNR is primarily formed by local resonances and quantum dots along the ribbon. The quantum dots are formed due to the width variation of the GNR. By superimposing a disorder potential giving rise to electron–hole puddles near the charge neutrality point,[55] the confinement gap ensures that Klein tunneling (from

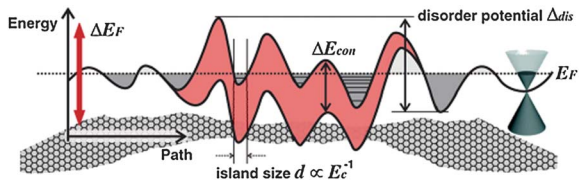

Fig. 6 Illustration of the potential landscape along the graphene nanoribbon allowing the formation of charged islands and quantum dots. (Reproduced from Stampfer *et al.*,[54] copyright 2009 by The American Physical Society.)

puddle to puddle) gets substituted by real tunneling. Within this model ΔE_F will depend on both the confinement energy gap due to island size (varying from location to location along the GNR) and the disorder potential.[54] This will result in nanoribbon properties dominated not by the specific physics of armchair or zigzag edge terminations, but by the degree of disorder in GNR dimensions and in the potential created by electron–hole puddles. Recent experimental data acquired on GNRs of 30 nm in width and of various lengths provided evidence in support of a model of nanoribbon behavior in which charged impurities in the vicinity of the ribbon create a disorder potential that, coupled with some small energy gap, breaks the ribbon up into isolated puddles of charge carriers that act as quantum dots.[56]

3.2. Nanoparticle lithography

Carrying out lithography with crystallographic orientation control demands techniques that inherently have crystallographic selectivity, while those techniques that do not, require that the crystallographic axes of the object are known with high precision. Lithographic processes based on scanning probe microscopy (discussed in Sections 3.3 and 3.4) belong to the second category; whereas various methods based on chemical reactions taking place at mobile nanoparticles belong to the first category. Although the movement of these nanoparticles cannot be controlled at our present level of knowledge, further research may reveal means to achieve this.[57] The topic of nanoparticle lithography was reviewed recently in detail,[19] so that only a brief enumeration of the most relevant results will be given here.

Several types of metallic nanoparticles have the capacity to cut trenches in graphite, one or several layers deep along selected crystallographic directions. Ni,[58,59] Fe,[60] and Co[61,62] have been reported to do so when heated in a hydrogen-containing atmosphere (see Fig. 7). In certain experiments, GNRs with a width as small as 10 nm were observed. Ag nanoparticles were found to promote the oxidation of graphene.[63] Very recently SiO_x nanoparticles were also reported to behave in a similar way like the transition metals.[64] The SiO_x nanoparticles were produced *in situ* by the annealing of graphene on SiO_2 in hydrogen-containing atmosphere at temperatures over 850 °C.

A point should be emphasized concerning the crystallographic selectivity of the reactions at mobile nanoparticles: the characteristic angles by which the trenches etched by the nanoparticles change direction indicate that the reactivity of graphene, few-layer graphite and graphite is different along different crystallographic directions of the basal plane. This will prove to be useful later for the discussion of pattern formation by controlled oxidation.

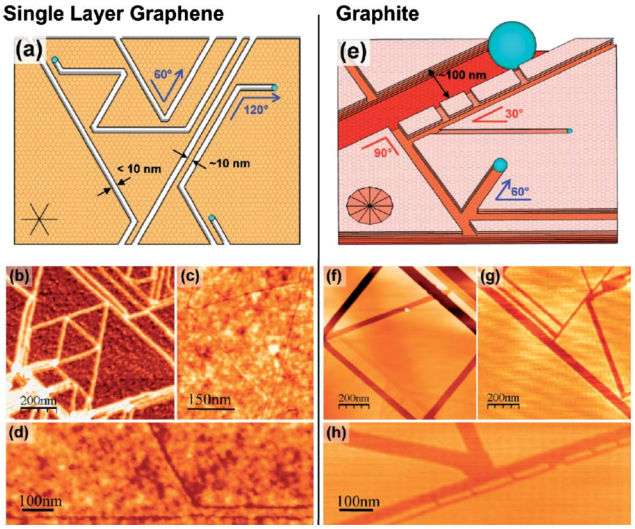

Fig. 7 Comparison of nanoparticle-assisted etching in graphene and graphite. (a) Key features of etching in graphene are chirality-preserving angles of 60° and 120°, avoided crossing of trenches leaving ~10 nm spacing between adjacent trenches and producing connected nanostructures, and trenches and nanoparticles with uniform width <10 nm. (b) AFM phase image of etched graphene with produced geometric nanostructures. The phase image obscures small details, making adjacent trenches appear to merge together. (c) AFM height image of equilateral triangle connected to three nanoribbons. (d) AFM height image of a trench which avoids crossing another trench running parallel to it (panels c and d color scale 0 to 1.7 nm). (e) Key features of etching in graphite and in few-layer graphene are chirality-changing angles of 90°, 150°, and 30°, in addition to 60° and 120°, trenches which merge, producing disconnected geometries, and trenches and nanoparticles of varying size (10–1000 nm). (f–h) AFM height images of etched graphite showing the previously mentioned features (color scale 0 to 7 nm). (Reprinted with permission from ref. 59. Copyright 2009 American Chemical Society.)

The most serious bottleneck of nanoparticle lithography is the very limited control on the placement of the nanoparticles and on the direction in which the etching will start.[19] Additionally, data are lacking regarding the edge roughness of the etched channels. Therefore one cannot exclude that these features exhibit a similar roughness at the atomic scale as those produced by e-beam lithography, which could represent a serious drawback regarding the possible applications. For example, a high-resolution TEM image in Fig. 1c of ref. 62 seems to indicate that even the channels looking regular at a lower magnification may have rough edges on the atomic scale.

3.3. Scanning tunneling lithography (STL)

A scanning tunneling microscope (STM)[65] is a characterization tool that routinely achieves atomic resolution imaging of various conducting surfaces. This very high lateral resolution follows from the quantum physics of the tunneling phenomenon[66] and essentially means that the tunneling channel in which the electrons flow from the tip to the sample is also of atomic width. Beyond high-resolution imaging, this instrument also offers the

opportunity to locally modify the sample surface.[67] Further advantages are that the crystallographic orientation of the sample is precisely known, after acquisition of an atomic resolution image, and the scanning tunneling spectroscopy (STS) operation mode immediately provides information on the electronic structure of the sample. In order to image and/or to modify a graphene layer with the STM, a conductive substrate is needed. The most convenient substrate is graphite itself, in particular the variety called Highly Oriented Pyrolytic Graphite (HOPG), which is also the substrate of choice for STM under ambient conditions. Quite early on, STM was used to modify the surface of HOPG.[68] In these first experiments it was already revealed that the writing of holes a few nanometres in diameter is possible only in the presence of water vapor condensed on the surface of HOPG.[69] Later on, it was proposed that, in fact, a localized chemical reaction takes place under the STM tip by the local decomposition of water under the well-confined electron flux emitted from the tip.[68] The etching process of the surface of bulk HOPG depends on several factors:[70] (i) there is a certain threshold voltage in the range of a few volts over which the modification of the sample surface starts; (ii) the magnitude of the threshold voltage depends on the scanning speed used; (iii) in turn the width and the depth of the lithographic features depend on the applied bias. In a systematic study,[70] it was shown that when keeping all other parameters constant except the bias voltage, the character and magnitude of the surface modifications change significantly in the voltage range from 2.74 V to 3.47 V. At the lower value, the first surface modifications were observed: small elevations on the sample surface, which are tentatively identified with C(O) type structures anchored to the sample surface. At the value of 3.47 V, the etching was already several atomic layers deep. On the other hand, the surface modification of bulk HOPG under UHV conditions does not start below a threshold voltage in the range of 8 V.[71] This clearly shows that the layer of adsorbed water has a very important role in the low voltage STM lithography of HOPG. Furthermore, by carefully controlling the gas environment during STL, the line width of the lithographic process may be improved.[72]

With a very careful tuning of the scanning parameters, GNRs of only one atomic layer thickness can be cut from the topmost layer of HOPG.[20] A bias of 2.4 V and a tip velocity of 2.0 nm s^{-1} are typical parameters, when used in ambient air, with a mechanically prepared Pt tip. GNRs with edges oriented along a desired crystallographic direction (a-GNR or z-GNR) can be cut. The edge roughness of the GNRs is comparable to lattice dimensions, as can be seen in Fig. 8. The crystallographic orientation of the GNR is determined prior to lithography by atomic resolution imaging. After the completion of the lithographic process, the electronic structure of the GNRs can be probed by STS. For the a-GNR of 2.5 nm in width (Fig. 8), a confinement gap of 0.5 eV was measured in good agreement with theoretical predictions. It is worth to point out that this gap value is large enough to allow the room temperature operation of nanodevices built from similar GNRs.

The complete removal of the topmost graphene layer after lithography demonstrates that the depth of the cut is indeed one-monolayer thick and the second layer of the HOPG sample is not damaged.[73] This feat may be achieved using for this nanoprocessing the very same STM tip as used for the lithography.

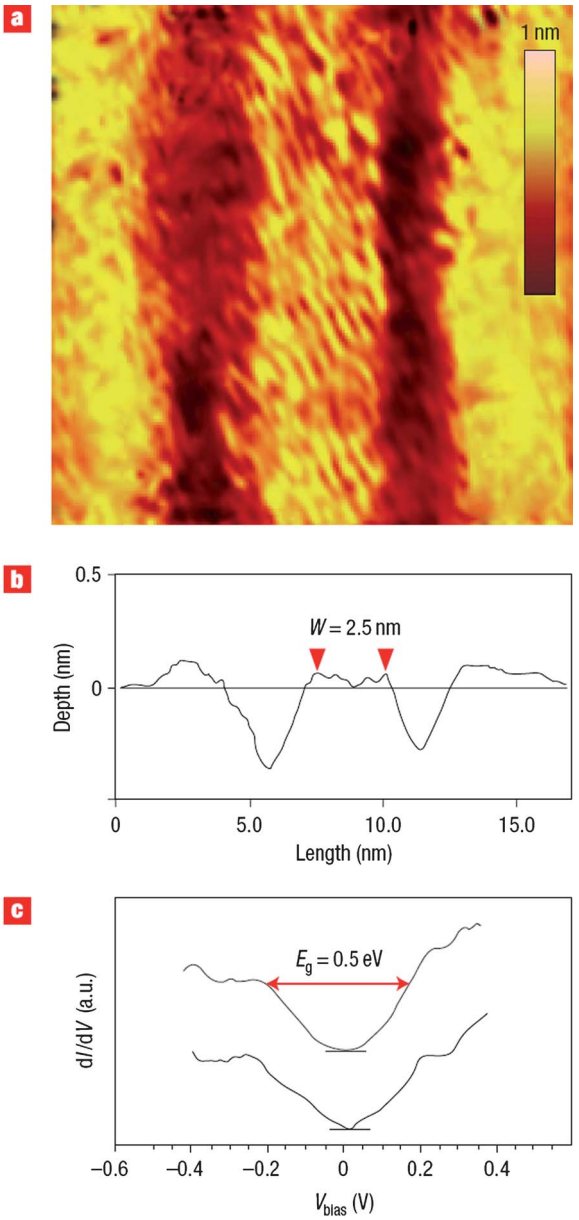

Fig. 8 (a) STM image (15 × 15 nm^2, 1 nA, 100 mV) of a 2.5 nm wide armchair GNR. The color scale bar encodes the height of the imaged features. (b) Line-cut of the STM image revealing the real width of the ribbon. (c) Representative STS spectra taken on the narrow ribbon showing an energy gap of about 0.5 eV (zero DOS marked by horizontal lines). (Adapted by permission from Macmillan Publishers Ltd: Nature Nanotechnology,[20] copyright 2008.)

The atomic scale roughness at the edges of the GNRs cut by STL produces some scattering at the edges and electronic interference patterns may appear in the atomic resolution STM images in the edge region. Even so, clear standing wave patterns are observed at room temperature due to the confinement of electron waves between the two edges of the GNRs.[20] The aspect of the observed standing wave patterns is dependent on the applied STM bias. Their presence shows that the edge disorder is low enough to preserve the coherence of the electron wavefunction at the length scale of the nanoribbon width.

To summarize the advantages of STL: (i) it makes possible the precise determination of the crystallographic orientation of the cut; (ii) the depth of the cut can be controlled with high precision; (iii) atomic resolution images can be taken immediately after the cutting process; (iv) the electronic structure of the GNR can be characterized by STS; (v) it is an important additional advantage that the method is resist free, it does not leave organic residues on the surface of graphene. The most serious disadvantages are that an electrically conducting substrate is needed and it is a slow, serial process, unless special multi-tip systems can be developed based on a principle similar to the one used in dip pen nanolithography.[74]

3.4. AFM lithography

The AFM[75] was developed primarily to compensate for the lack of capacity of the STM to image non-conducting surfaces. AFM lithography of HOPG[76] and of graphene[77–83] is based on a local oxidation reaction. It can be regarded as a variation of the STL method in which the atomically sharp STM tip is replaced by an AFM tip with a conductive metallic coating and apex radius of curvature in the range of tens of nanometres at best. The cutting process itself is the same as in the case of STL, namely, it is based on the decomposition of the water layer adsorbed on the surface.[76,84] During the electrochemical oxidation of HOPG by AFM, the oxidative species (OH^-, O^-) react with the sp^2 carbon and convert it to sp^3 with hydroxyl and epoxy functional attachments or to CO and CO_2 when the oxidation is complete.[78,85] But as the tip has a larger radius of curvature and the flowing current is not a tunneling current—so it lacks the exponential dependence on the tip-sample distance—the width of the current channel is much larger as compared with the STL and the individual tip shape has a significant influence on the cut width.[86] A clear advantage of the AFM lithography is that it does not need a conductive substrate for feedback like the STM; therefore working on insulting substrates is possible.

As a likely consequence of the different mechanisms of current flow in the STL process and the AFM lithography, there is a much wider scatter in the voltage values, from −5 to −35 V, under which the cutting process is initiated,[86] than in the case of STL. Moreover unusual features may be produced, like bumps attributed to the incorporation of oxygen in the carbon network without complete oxidation.[77] An alternative explanation could be the deposition of material from the metal coating of the conductive tip. So-called pseudo-cuts have been reported recently,[86] which appear as real cuts in the AFM images, although the electronic system of the graphene remains intact. The pseudo-cuts can be distinguished from real cuts in the SEM at a low accelerating voltage (500 V), Fig. 9.

The best resolution obtained so far yields features of 14 nm, whereas the typical feature size is in the range of 30 nm up to 100 nm, depending on the individual tip shape.[86] These results were obtained with non-coated, doped Si tips on mechanically exfoliated mono- and bi-layer graphene on SiO_2. For cutting, the AFM was operated in contact mode (C-AFM). A threshold value was found $|V_{thresh}|$ which has to be exceeded ($|V_{tip}| > |V_{thresh}|$) in order to produce real cuts[86] (the threshold value may vary from −3.5 V to −5 V depending on the tip used). When the $|V_{thresh}|$ value is exceeded by the voltage applied to the tip, the current flowing through the tip drops to zero, opposite to the case when voltages below the threshold value are applied. The pseudo-cuts obtained in the latter conditions may vanish in a few hours or days in ambient atmosphere. At voltage values over the threshold, the current flowing between the tip and the graphene falls to zero and real cuts are produced. Micro-Raman and electric force microscopy data indicate that the edges of the features written by AFM lithography in sp^2 carbon layers are functionalized by oxy functional groups.[85]

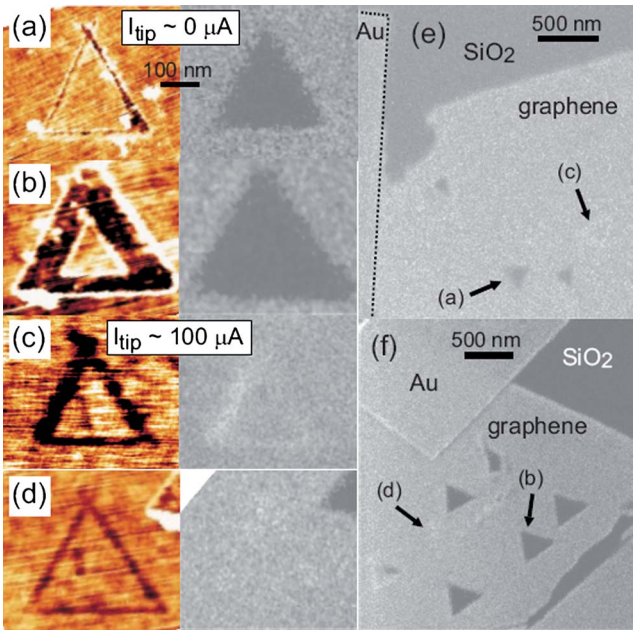

Fig. 9 (a and b) AFM (left) and SEM (right) images of two triangles cut of graphene on SiO_2 with $|V_{tip}| > |V_{thresh}|$ such that the tip current, $I_{tip} \approx 0$ during cutting. (c and d) AFM (left) and SEM (right) images of two triangles cut with $|V_{tip}| < |V_{thresh}|$ such that $I_{tip} \approx 100$ mA during cutting. (e and f) SEM images of the areas of the graphene flake on which the triangles were cut. The arrows indicate the locations of the triangles shown in panels (a)–(d). (Reprinted with permission from ref. 86. Copyright 2011, American Institute of Physics.)

A different variety of AFM lithography can be performed using the AFM tip as a stylus to scratch the graphene layer.[87,88] Because graphene tends to fold itself when the AFM tip is scratching it, graphene on the SiO_2/Si system was found to be impractical. However, a thin layer of PMMA intercalated between the graphene and the SiO_2 helps to avoid this problem.[87] The smallest gap width could be down to 10 nm using AFM tips made of silicon nitride instead of silicon. Unfortunately, the edge of the scratched channels is very rough, so that there are only moderate chances that this method could be successfully used to produce GNRs. In a recent experiment, copper-phthalocyanine was deposited in the gaps produced by scratching; photoconductive signals and transistor characteristics were measured, but in these measurements the graphene acted only as an electrode.[87] The serious disadvantage of this nanolithographic method is the need for a PMMA underlayer to avoid graphene from folding under the AFM tip pressure. This brings back all the problems connected with organic residues remaining on or under the graphene.

3.5. Carbothermal etching (CTE)

Carbothermal etching (CTE), a combination of the kind of AFM lithography in which the AFM tip is used as a stylus (see the previous section) and the crystallographic selective chemical reaction taking place at mobile nanoparticles, is used for etching channels in graphene (see Section 3.2.). It is based on the solid-phase chemical reaction between carbon atoms with dangling bonds and the SiO_2 substrate.[21] The oxygen needed for the oxidation of the graphene layer is extracted from the SiO_2 substrate. As already discussed above, under certain annealing conditions, the graphene may interact with its substrate to produce nanoparticles and chemical reactions between these and the graphene layer.[64] During the oxidative thinning of FLG flakes down to a single graphene layer, the latter can interact with the SiO_2 substrate differently as multilayers do.[89] Indeed, as shown in Fig. 2d of ref. 89, the edges of the graphene layer recede while leaving behind a depression on the substrate. This is in agreement with earlier observations that SWCNTs may produce trenches on the SiO_2 surface.[90]

During CTE the annealing of mechanically exfoliated graphene on SiO_2 is carried out in Ar atmosphere at the temperature of 700 °C.[21] Under these conditions the oxidation takes place only at the already existing graphene edges according to the following reaction:[91]

$$SiO_2(sol) + C(edges) \Rightarrow SiO\uparrow + CO\uparrow$$

As both reaction products are volatile at the annealing temperature, they are removed by the flow of Ar gas. Therefore, a depression is created where the graphene edge has reduced the substrate silica to SiO. The reaction is a solid-phase one that exhibits clear indications of crystallographic selectivity. The initially round shape of the pit formed during the oxidation of the graphene at 500 °C in air is transformed to a well-shaped, regular hexagon.[21] Furthermore, both atomic resolution STM images[21] and Raman mapping[30] confirm that the termination of the edges produced by CTE is precisely zigzag.

As compared with the crystallographically selective nanoparticle etching and the AFM lithography, which uses the tip for scratching, the major differences are as follows: (i) the AFM tip is not moved along a line, it is used only to produce defects at a certain point which will initiate the reaction; (ii) the crystallographically selective chemical reaction can start only at those points where the defects have been created by the AFM indentation.[21] These differences allow for the realization of *a priori* planned patterns, like antidot lattices of holes with precisely zigzag edges, Y-junctions (see Fig. 10), *etc.*[21]

The zigzag-edged hexagonal holes produced by CTE made it possible for the first time the experimental confirmation of the theoretical predictions concerning the behavior of graphene edges with well-defined structure.[92] The narrowest zigzag nanoribbon produced so far by CTE has a width of 30 nm.[93] The main advantage of the method is not the easy production of narrow GNRs—the starting point of the reaction by AFM indentation has to be placed with great precision for this—but resides in its ability to produce complex nanoarchitectures.

Recently, a hydrogen plasma-based etching technique has been shown to also produce zigzag-edged graphene nanostructures on top of HOPG- and SiO_2-supported graphene.[31]

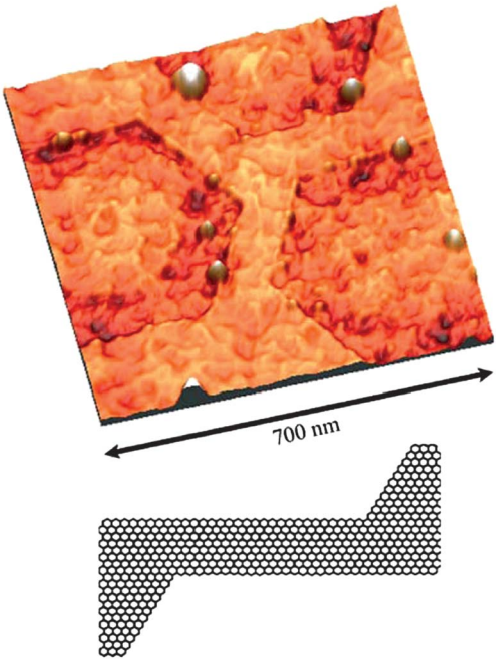

Fig. 10 A "Y" junction of three graphene nanoribbons, with the ribbons having widths of 93, 100, and 101 nm (starting from the upper left ribbon, going clockwise). The inset at the bottom shows a scheme of the corresponding atomic structure. (Reprinted with permission from ref. 21. Copyright 2010, Springer.)

This process also shows good crystallographic selectivity, although the roughness of the zigzag edges prepared by CTE and plasma etching has not been directly compared yet.

3.6. Edge engineering

The properties of graphene edges, their characterization and the question of edge engineering have been reviewed recently in detail.[94] However, the narrowing down of GNRs and edge quality is a crucial issue for any graphene nanoarchitecture, which justifies the brief reviewing of a few recent results here.

A high-temperature, slow and well-controlled etching procedure was reported for nanoribbons and other more complex shapes, initially produced by e-beam lithography (using Al mask instead of resist), then narrowed down from ~20 nm to about 8 nm in width by using an NH_3, O_2 mixture in argon, without creating defects in the basal plane of graphene.[95] As a result of the presence of bond disorders and functional groups at the edges of the graphene, the chemical reactivity of the edge carbon atoms is higher than that of the perfectly bound sp^2 carbon atoms in the basal plane. The lack of defects created in the basal plane was checked by Raman mapping.[95] Parallel arrays of ~8 nm wide GNRs were used to produce FETs with an on/off ratio of ~50 and with 'on' currents far exceeding those of single-ribbon devices. The edge roughness caused by random fluctuations in the lithographic and etching process was found to be smaller than 5 nm,[95] this seems to set a limit for the width of continuous GNRs that can be produced using this procedure.

A lower temperature (300 °C) hydrogen plasma etching procedure was developed recently.[96] The etching rate, as

measured by AFM, for single-layer graphene and few-layer graphene ($g \geq 2$ layers) are 0.27 ± 0.05 nm min^{-1} and 0.10 ± 0.03 nm min^{-1}, respectively. The reported difference of etching rates is in agreement with the difference found in the behavior of single-layer graphene and FLG when oxidized on SiO_2.[89] Raman spectroscopic mapping revealed no D band in the planes of single-layer or few-layer graphenes after the plasma reaction, confirming the selective etching at the graphene edges without introducing defects in the basal plane.[96] GNRs could be narrowed down to the range of 5 nm and FETs with an on/off ratio of ~1000 were produced.

Using low-voltage (60 keV) scanning transmission microscopy (STEM), single atom spectroscopy experiments were carried out at the edges of graphene flakes mechanically cleaved from HOPG.[97] STEM annular dark field (ADF) images indicated that the graphene flakes had open and active edges[98] and that the edges are steadily etched by the incident electron beam when the probe-scanning is repeated in the same region. Energy-Loss Near-Edge fine Structure (ELNES) spectra of individual carbon atoms in triple coordination, double coordination and single coordination were recorded. The spectra show clear differences in the electronic structure of the three types of edge atoms. The single coordinated atoms are rather unstable under the experimental conditions. The open edges involve both single- and double-coordinated carbon atoms, but their specific edge states are completely localized at the atomic level. This localization was already demonstrated in 2001 by both STM and electronic structure calculations for edge-terminated layers of graphite.[99] Even for triple coordinated carbon atoms, slight electronic structure modification may exist near the edge region, but it vanishes after 1.5 nm from the edge front. This result comes from Electron Energy Loss Spectroscopy (EELS) performed along a line normal to the graphene flake edge, revealing that atoms at a distance of 1.5 nm from the edge show a normal sp^2 spectrum.[97] It is concluded that the properties of GNRs with a width smaller than ~3 nm might be governed by edge effects.[97]

STM was used to obtain some information regarding the general orientation of the edges of a micromechanically cleaved graphene flake on SiO_2.[100] In order to make possible the STM imaging, the graphene was connected to metallic contacts. STM imaging right in the edge region is not possible as the STM tip moving on the flake edge would immediately crash into the oxide. Nevertheless, at some distance from the edge, atomic resolution images may be recorded, which give information on the general direction of the edge, but are unfortunately not suitable to reveal the real atomic structure of the edge.

4. Bottom-up nanostructuring

4.1. Epitaxial GNR growth on SiC

The epitaxial growth of graphene on h-SiC is a method for graphene production[101] by which wafer-scale graphene transistors operating at 100 GHz can be produced.[102] Unfortunately due to the absence of a band gap, these transistors are not suitable for digital applications. Therefore, the direct, bottom-up growth of epitaxial GNRs on SiC is extremely promising. The procedure is based on the self-organized growth of graphene nanoribbons on a templated silicon carbide substrate prepared using scalable photolithography and microelectronics processing.[103] This may avoid the edge damage as a result of post-processing. The achieved ribbon width of 40 nm remains within the possibilities of e-beam lithography, but with further work, the GNR width may be reduced. The prototype GNR devices exhibit an on/off ratio of 10 at 4 K.[103] The procedure allowed the simultaneous fabrication of top-gated FET devices with a density of 40.000 devices per cm^2.

The procedure is based on the observation that the morphology of epitaxial graphene on SiC is highly influenced by the underlying SiC structure. $(1\bar{1}0n)$ facet formation may be induced by pre-processing of the SiC. Controlled facets are achieved by the photolithographic definition of nickel lines on a SiC substrate perpendicular to the $\langle 1\bar{1}00 \rangle$ direction; these lines are transferred into the SiC by a fluorine-based reactive ion etch (RIE). The critical factor defining the width of the GNR will be the depth of the etch (see Fig. 11).[103] The formation of the $\langle 1\bar{1}00 \rangle$ facet is carried out after the removal of the Ni mask and cleaning in the temperature range of 1200–1300 °C in a vacuum of 10^{-4} torr, while the GNR growth takes place at around 1450 °C in a time interval of 10 minutes, after which the sample was cooled down.

4.2. Surface directed assembly of organic molecules

It may seem surprising that the first graphene nanoribbons—of only one benzene ring width—both with armchair and with zigzag edge have been synthesized more than 50 years ago by organic chemists.[104] Both armchair (*para*-hexaphenyl or sexiphenyl)[105] and zig-zag (hexacene and heptacene)[106] GNRs were synthesized decades ago. Sexiphenyl (armchair edge) and heptacene (zig-zag edge), both have the width of only one benzene ring, sexiphenyl has a band gap of the order of 3.2 eV,[107] while heptacene (a polyacene with $n = 7$ benzene rings) has a band gap of only 1.5 eV.[108] Theoretical calculations show that the band gap of polyacenes shrinks rapidly to zero as the number of benzene rings increases to 10.[109] This is very similar to the behavior expected from a zigzag GNR. The gap of oligophenylenes shows very little change from 6 to 12 rings,[110] that is, they behave like armchair GNRs. Unfortunately the production of polyacenes and oligophenylenes of more hexagonal units seems to be hindered by the possibilities of organic synthesis.

Taking the inspiration from organic chemistry for the preparation of GNRs, a promising research direction is the surface-directed assembly of organic molecules. Fig. 12 sketches the basic GNR fabrication steps for a prototypical armchair ribbon, having a width of 7 carbon chains, obtained from 10,10′-dibromo-9,9′-bianthryl precursor monomers.[111]

It is beyond the scope of the present review to discuss the fine details of the organic chemistry taking place on the Au(111) surface in the temperature range of 200 °C and, later on, the second reaction step occurring at 400 °C. Armchair-edged GNRs of about 2 nm in width and around 30 nm in length were produced, as demonstrated by STM images and by simulations. Other more complex shapes, like Y-junction type nanoarchitectures composed of "chevron-type" elements, were also produced using different precursors as compared with the case of a-GNRs.

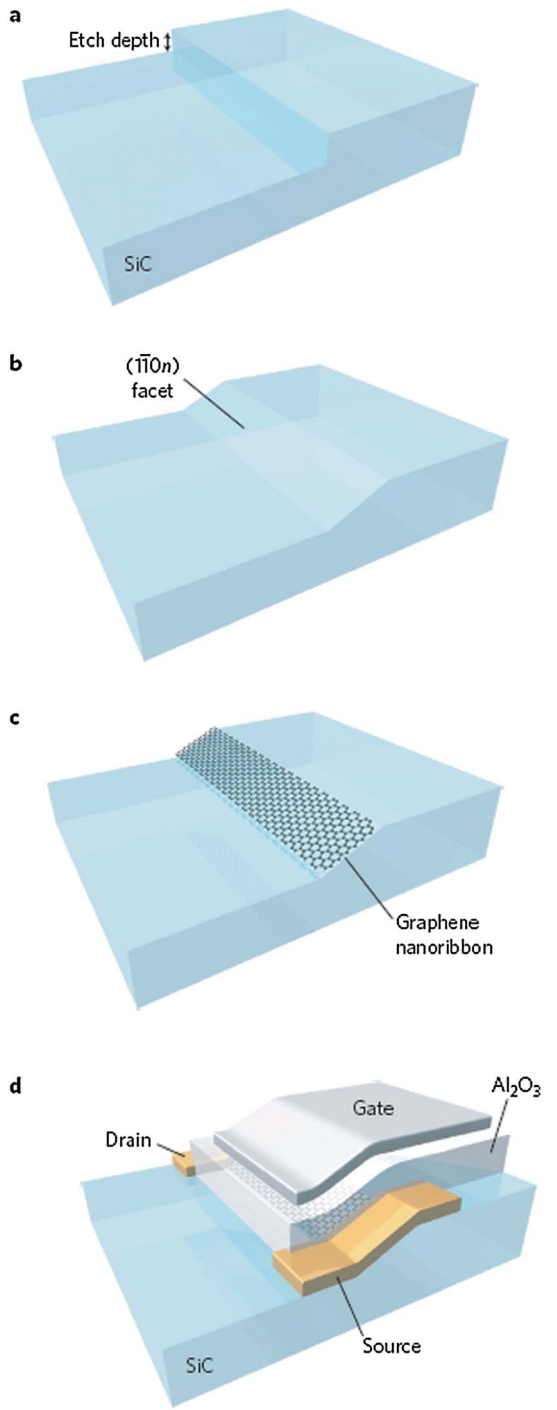

Fig. 11 Process for tailoring of the SiC crystal for selective graphene growth and device fabrication. (a) A nanometre-scale step is etched into SiC crystal by fluorine-based RIE; (b) the crystal is heated to 1200–1300 °C (in low vacuum), inducing step flow and relaxation to the (1$\bar{1}$0n) facet; (c) upon further heating to ~1450 °C, self-organized GNR forms on the facet; (d) complete device with source and drain contacts, graphene nanoribbon channel, Al_2O_3 gate dielectric and metal top-gate. (Reprinted with permission from Macmillan Publishers Ltd: Nature Nanotechnology (ref. 103), copyright 2010.)

Several other possible routes of organic synthesis that may yield graphene type structures are reviewed in ref. 112.

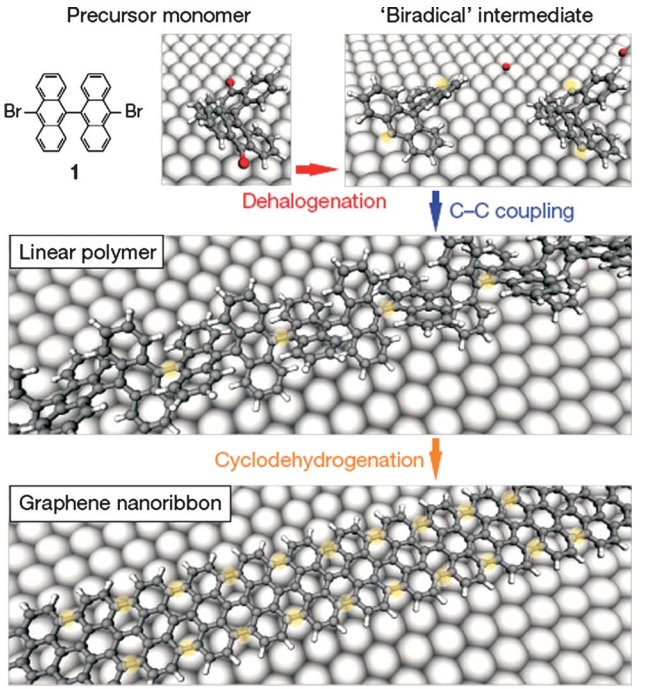

Fig. 12 Bottom-up fabrication of atomically precise GNRs. Basic steps for surface-supported GNR synthesis, illustrated with a ball-and-stick model of the example of 10,10′-dibromo-9,9′-bianthryl monomers. Grey, carbon; white, hydrogen; red, halogens; underlying surface atoms shown by large spheres. Top: dehalogenation during adsorption of the di-halogen functionalized precursor monomers. Middle: formation of linear polymers by covalent interlinking of the dehalogenated intermediates. Bottom: formation of fully aromatic GNRs by cyclodehydrogenation. (Reprinted with permission from Macmillan Publishers Ltd: Nature (ref. 111), copyright 2010.)

5. Applications

Some of the most widespread applications like the GNR-based FETs, which are also used for characterizing the charge transport properties of the realized GNRs,[113] were already mentioned above and will not be discussed in more detail here.

5.1. Graphene nanomeshes by block copolymer lithography

Block copolymers are well known for forming regular nano-patterns.[114] A graphene nanomesh (GNM) is a single- or few-layer graphene into which a high-density array of nanoscale holes are introduced (see Fig. 13).[115] The distribution of the holes is not completely regular (either in the size of holes or in the distance between them), but two structural parameters can be defined: the average "periodicity", defined as the center-to-center distance between two neighboring nanoholes, and the "neck width", defined as the average of the smallest edge-to-edge distance between two neighboring nanoholes in the nanomesh. A poly (styrene-*block*-methyl methacrylate) (P(S-*b*-MMA)) block copolymer thin film with cylindrical domains normal to the surface was fabricated and used as the etching template, and a CHF_3-based RIE process, followed by oxygen plasma etching to induce holes into a graphene layer.[115] The GNM layer was used to produce FET devices.

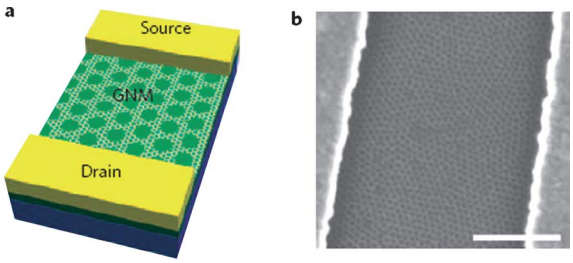

Fig. 13 (a) Schematic of a GNM-FET. The device is fabricated on a heavily doped silicon substrate with 300 nm SiO_2 as the gate dielectric. (b) SEM image of a GNM device made from nanomesh with a periodicity of ~39 nm and a neck width of ~10 nm. Scale bar, 500 nm. (Reprinted with permission from Macmillan Publishers Ltd: Nature Nanotechnology (ref. 115), copyright 2010.)

The GNMs are viewed as a highly interconnected network of GNRs. Narrow neck width is needed to gain enough band gap to offer both sufficient gate response and high on–off ratio; a denser mesh structure can enable higher current delivery. On/off ratios in the range of 10 to 100 have been obtained for GNMs with different neck widths.[115] The opening of the conduction band gap in the GNM structure is attributed to a combination of multiple factors, including lateral quantum confinement and a localization effect resulting from edge disorder, such as variable edge roughness or absorbed species in the oxygen plasma etching process.

A very similar procedure was reported to achieve features sizes <10 nm in HOPG. A thin film of the cylinder-forming diblock copolymer poly(sytrene-*block*-methyl methacrylate) [P(S-*b*-MMA)] was used as a template. The layer consisted of a thin film of a random copolymer of methyl methacrylate (MMA), styrene (S) and glycidyl methacrylate (GMA), P(S-*r*-MMA-*r*-GMA), which acted as a non-preferential or neutral layer. An intermediate 10 nm SiO_2 layer was used between the HOPG and the polymer layer to avoid nonuniform coating and dewetting.[116] The polymer film was annealed (220 °C, vacuum, 3 h) resulting in a 25 nm thick film. A hexagonal array of vertically oriented PMMA cylinders was observed at this stage (Fig. 14a). The sample was then exposed to UV illumination (1000 mJ cm^{-2}) to selectively degrade the PMMA cylinders. After the processing steps shown in Fig. 14, a single sheet of graphene was mechanically exfoliated onto 86 nm SiO_2/Si (p++) wafers. Measurements were performed under ambient conditions, the conductance on/off modulation for gate biases in the range of ±30 V was 7.3 ± 1.9 at room temperature.[116] Subsequent O_2 plasma etching could increase the on/off ratio in the range of 40. Unfortunately, after O_2 plasma etching, the devices demonstrated a hole mobility of only around 1 cm^2 V^{-1} s^{-1} at low drain bias (<10 mV) at room temperature.[116]

5.2. Antidot lattices

A more regular version of the GNMs are the so-called graphene antidot lattices.[117–119] An antidot lattice consists of a periodic array of holes that causes a band gap to open up around the Fermi level, transforming graphene from a semimetal to a semiconductor.[117] The magnitude of the gap is highly sensitive to the size and separation of the holes. The lattice consists of hexagonal

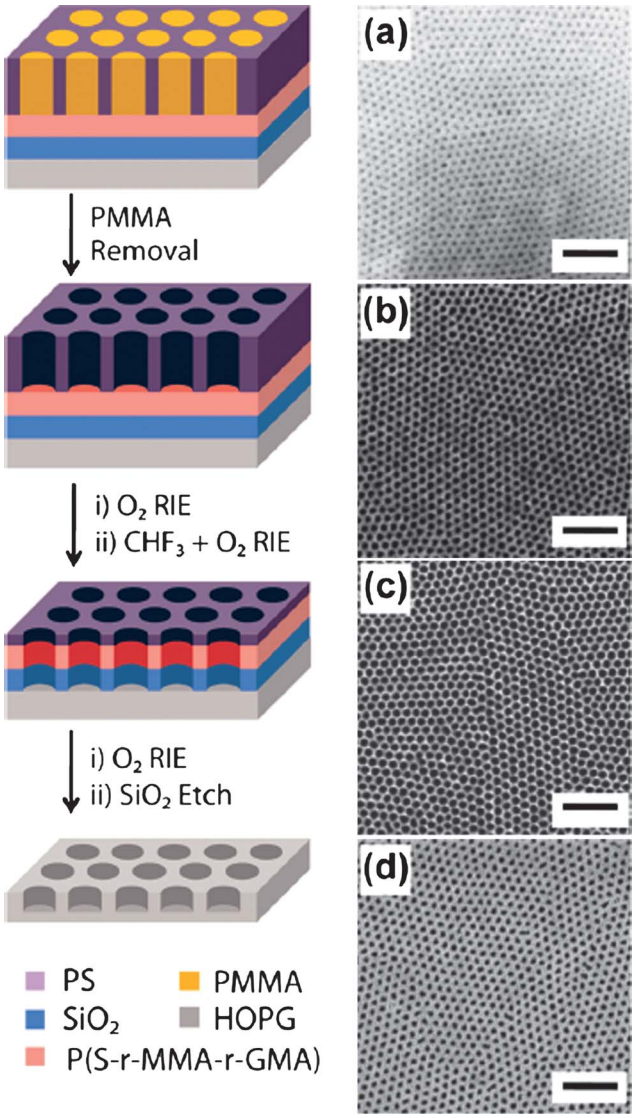

Fig. 14 Scheme depicting the fabrication of nanoperforated HOPG using block copolymer lithography and the corresponding top-down SEM images of (a) vertically oriented PMMA cylinders in a block copolymer thin film obtained by thermal annealing, (b) residual polystyrene honeycomb template obtained after selective PMMA removal with UV irradiation, (c) etched structures after O_2 followed by CHF3 + O_2 plasma RIE resulting in the etching of the random copolymer mat and the oxide buffer layer, respectively, and (d) nanoperforated HOPG resulting from the final O_2 plasma RIE and the removal of the oxide buffer by HF solution. Scale bars = 200 nm. (Reprinted with permission from ref. 116. Copyright 2010, American Chemical Society.)

unit cells, as shown in Fig. 15b, in which a roughly circular hole is created. Also of importance are the total number of sites in the unit cell N_{total} (equal to the number of atoms before the hole is made) and the number of removed atoms $N_{removed}$. For example, for the {7,3} lattice $N_{total} = 294$ and $N_{removed} = 60$. The calculated gap value of the nanoarchitecture scales roughly linearly with $N^{1/2}_{removed}/N_{total}$; E_g values in the range of 1 eV are calculated for $N^{1/2}_{removed}/N_{total} = 0.04$.[117]

Intentional defects in the antidot lattice can be produced by leaving one or several unit cells intact, *i.e.*, without a hole. Such

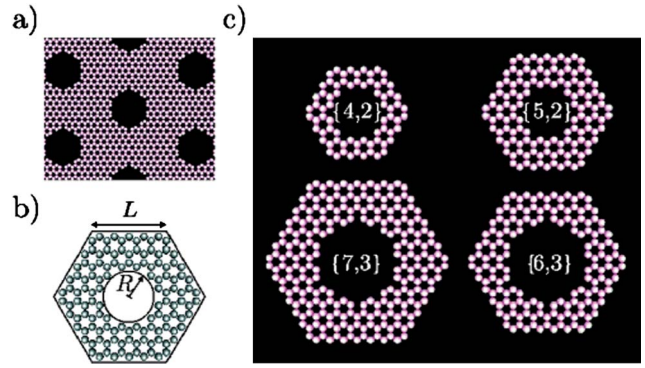

Fig. 15 Illustration of the triangular antidot lattice (a) with a unit cell characterized by side length L and hole radius R (b). In (c), several examples with corresponding $\{L;R\}$ parameters are shown, both L and R are measured in units of the graphene lattice constant $a = 0.246$ nm. (Reproduced from Pedersen *et al.*,[117] copyright 2008 by The American Physical Society.)

defects may support localized electronic states and may consequently be utilized for electron spin qubits.[117] Hole shape may play an important role in determining the properties of such nanoarchitectures, the replacement of the circular perforation with a triangular one having zigzag edges produces a dispersionless "metallic" band at the Fermi level.[120] Antidot lattices with such triangular perforations would lead to additional interesting features in the optical response, such as controllable transparency windows. In the case of antidot lattices with circular holes, it is found that the lattice geometry plays a crucial role on the size of the band gap: the triangular arrangement displays always a sizable gap, while for the other types (rectangular, the rotated triangular, and the honeycomb) only particular hole separations lead to a large gap.[121]

Calculations show that antidot lattices are two-dimensional, dipole-allowed, direct-gap semiconductors. This will be important for possible optoelectronic applications, including light emission and detection. Also, experimental detection of band gaps using infrared spectroscopy should be feasible.[120]

The effects of hydrogen passivation and of vacancies in the inner edge of the antidots were investigated theoretically. Passivation was found to increase the band gap, whereas the presence of carbon vacancies along the hole edges was shown to induce midgap bands.[122] Such states may be responsible for the relatively low values of band gaps opened in graphene nanomeshes, where the edges of the holes have a random structure.

Various antidot patterns have been prepared by e-beam lithography followed by reactive O_2 ion etching, or low-energy Ar ion etching (350 eV).[123] The graphene flakes were prepared by micromechanical cleavage onto a SiO_2 substrate. The lattice periods were varied from 90 to 400 nm, the antidot diameters from 54 to 150 nm, while the neck widths were in the range of 1.3 to 4 μm. The transport properties were measured in a ^{4}He-cryostat at temperatures between 1.6 and 48 K using lock-in techniques with an ac bias current of 10 nA or lower. The antidot lattices showed a high-resistance state around the Dirac point, with an on/off ratio of about 100 at 1.6 K. In large-period lattices, a well-defined quantum Hall effect is observed; at smaller antidot spacings, the quantum Hall effect gradually disappears. Lattices with narrow constrictions between the antidots behave as networks of GNRs, showing a high-resistance state and a transport gap of a few mV around the Dirac point. Weak localization and intervalley scattering are observed. The etched boundaries of the antidots are found as the obvious source of intervalley scattering.[123]

Magnetism in graphene-type materials has been reviewed recently.[124] Rich magnetic physics is predicted for graphene superlattices with zigzag edges (both dot and antidot lattices).[125–127] Unfortunately, the experimental data to be compared with theoretical predictions are lacking.

5.3. z-GNR with antidot lattices

An even more challenging nanoarchitecture from the point of practical realization is the z-GNR with an incorporated antidot lattice.[128] Calculations of band structure and transport features show that an antidot lattice could turn the semi-metallic graphene into a semiconductor. The size of the band gap can be tuned by the position of the antidots and the distance D between the two nearest antidots. For a finite superlattice with N antidots and a large D, a group of $(N - 1)$ splitting resonant peaks and transmission-blockade regions appear alternately in the conductance spectrum. This indicates the formation of minibands and minigaps.[128]

5.4. Single electron transistor (SET)

Single electron transistors could constitute the ultimate computing device operating with electrons. Different SET devices have recently been produced from graphene.[54,129–131] The core element of the SET is a graphene quantum dot (QD). At large sizes (>100 nanometres), the QDs behave as conventional single-electron transistors, exhibiting periodic Coulomb blockade (CB) peaks. For quantum dots smaller than 100 nanometres, the peaks become strongly nonperiodic, indicating a major contribution of quantum confinement. The distance between CB peaks is determined by the sum of charging and confinement energies $\Delta E = E_c + \delta E$, and the latter contribution becomes dominant for devices with $D < 100$ nm.[129]

All of the reported SETs have been realized in micromechanically cleaved graphene on a SiO_2 substrate processed by e-beam lithography and subsequent O_2 plasma etching. Graphene QDs with features as small as 10 nm could be fabricated reliably using the lateral "under-etching" process. For even smaller dimensions, the irregularities in PMMA ~5 nm (ref. 132) become comparable in size with the designed features, thus making their shape uncertain.[129] Devices narrowed down to nanometre width exhibited on/off conduction state even at room temperature (Fig. 16).

The width variations in the two GNRs or nanoconstrictions connecting the central QD to the leads have a significant influence on the properties of the SETs. A graphene SET[130] was used to detect individual charging events in an etched GNR placed near the SET.[54] Experimental evidence has shown that the transport gap in an etched graphene nanoribbon is primarily formed by local resonances and quantum dots along the ribbon. Quantum dots along the nanoribbon can arise in the presence of

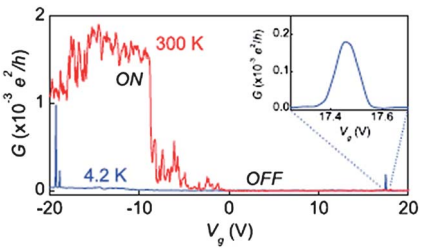

Fig. 16 Electron transport through a controllably narrowed device with a minimal width of only ~1 nm as estimated from its $\Delta E \approx 0.5$ eV. Its conductance can be completely pinched-off even at room T. Fluctuations in the on-state at room temperature are time dependent (excess noise). At low T, the on-state exhibits much lower G, and the noise disappears. Occasional transmission resonances can also be seen as magnified in the inset. (From ref. 129. Reprinted with permission from AAAS.)

a quantum confinement energy gap combined with a strong bulk and edge-induced disorder potential (see Fig. 6).

5.5. Nanconstriction transistor

A different method as compared to conventional e-beam lithography to pattern monolayer graphene nanoconstriction field effect transistors (NCFETs), with critical dimensions below 10 nm, is reported in ref. 133. NCFET fabrication is enabled by the use of feedback controlled electromigration (FCE)[134] to form a constriction in a gold etch mask that is first patterned using conventional lithographic techniques. The use of FCE allows the etch mask to be patterned on size scales below the limit of conventional nanolithography.[133] The FCE process was conducted on an e-beam patterned gold structure on top of conductive graphene resulted from micromechanical exfoliation. During FCE, a slowly ramped voltage is used to electromigrate gold out of a constriction in a "bow tie" structure. In the typical literature on FCE, this process is continued until a tunneling gap is opened[134] when the production of a NCFET is intended, the process is stopped while a small ~10 nm junction of gold is left in the middle of the structure. Following FCE, oxygen plasma etching is used to remove graphene regions that are unprotected by the gold, and then the sample is immersed in a KI/I_2 gold etch solution to wash away the remaining gold structure. A sharp increase is observed in the on/off ratio of the NCFET (up to 1000 at room temperature) with the reduction of the width of the constriction. NCFETs with constriction widths in the range of 8–150 nm were fabricated, moreover, the metal contacts to the NCFETs are much larger than what is possible for chemically derived nanoribbon devices and are thus "bulk" contacts whose resistance is much smaller than that of the graphene channel. This allows a direct measurement of the electrical characteristics of the graphene nanoconstriction with only a minor contribution from any contact barriers.

5.6. Spin filter ("valleytronics")

Another possible application was proposed for more regularly shaped graphene nanoconstrictions. A so-called valley filter is based on a z-GNR sandwiched between two broader contacts (Fig. 17). A key ingredient for "valleytronics" would be a controllable way for the charge carriers to occupy a single valley in graphene, thereby producing a valley polarization.[135] Conduction in GNRs (long and narrow ballistic strips) may support a propagating mode arbitrarily close to the Dirac point, and this mode lacks the valley degeneracy of modes that propagate at higher energies. For a-GNRs, this lowest propagating mode is constructed from states in both valleys, but for z-GNRs only a single valley contributes.[136] The constriction is regarded as the quantum point contact[137] in the graphene sheet. The orientation of the graphene lattice is such that the constriction has zigzag edges along the direction of current flow. In this case, the two valleys in graphene can be addressed individually as independent internal degrees of freedom of the conduction electrons. The polarization of this valley filter can be inverted by locally raising the Dirac point in the region of the constriction, by means of a gate voltage, such that the Fermi level lies in the conduction

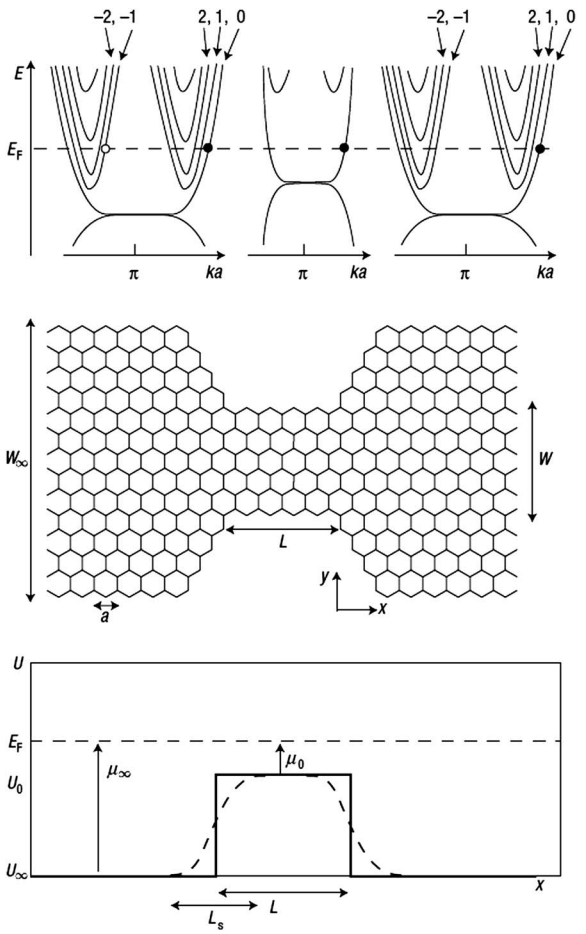

Fig. 17 Schematic diagram of a so-called valley filter. Middle panel: honeycomb lattice of carbon atoms in a strip containing a constriction with zigzag edges. Top panel: dispersion relation in the wide and narrow regions. An electron in the first valley (modes $n = 0,1,2,\ldots$) is transmitted (filled circles), whereas an electron in the second valley (modes $n = -1,-2,\ldots$) is reflected (open circle). Bottom panel: variation of the electrostatic potential along the strip, for the two cases of an abrupt and smooth potential barrier (solid and dashed lines). The polarity of the valley filter switches when the potential height, U_0, in the constriction crosses the Fermi energy, E_F. (Reprinted with permission from Macmillan Publishers Ltd: Nature Physics (ref. 135), copyright 2007.)

bands in the wide regions and in the valence band inside the constriction.[135]

Later on, other more complex valleytronic devices were proposed based on theoretical calculations, exploiting optical analogues,[138] double bended z-GNR/a-GNR/z-GNR,[139] or straight a-GNR/z-GNR/a-GNR[140] structures. Along this line of valleytronics, another approach is proposed for electron beam manipulation in the graphene layers by properly shaped z-GNR and a-GNR strips attached to large graphene sheets or complex nanopatterns carved from graphene.[141] These complex nanopatterns named Hetero-Dimensional Graphene Junctions (HDGJs) when injected with hot electrons, whose energy lies within the trigonal warping region, will split or collimate electron beams depending on the type of the GNR (a-GNR or z-GNR) used for current injection.[141] Unfortunately the experimental realization of valleytronic devices has not yet been reported.

6. Summary and outlook

The overview of methods for nanoscale patterning clearly shows that, due to the particular electronic structure of graphene, the development of new tools able to control, at the same time, both the crystallographic orientation of the graphene edges and their atomic scale structure is a cornerstone for future graphene-based nanoelectronics and spintronics. The two competing approaches, namely, the top-down approach of materials science and the bottom-up approach of chemistry, both have their drawbacks and advantages.

The various lithographic methods mostly avoid the problems faced when one has to place a nano-object with nanometric precision to the location where it has to perform a certain task (for example, a component in an electrical circuit). This type of problem is well known from more than one and half decades of carbon nanotube research. On the other hand these methods face three serious bottlenecks:

• the micromechanically cleaved graphene, while suitable for fundamental research, is clearly unsuitable for large-scale practical applications; the other kind of widely used graphene samples, those produced by CVD, presently still bring along an additional complication because of the grain boundaries incorporated in them.

• the various kinds of e-beam lithography combined with different post-lithographic narrowing techniques leave behind an unacceptable level of edge disorder, which is transmitted further during the chemical narrowing of GNRs, setting a limit in the range of 5 nm for such GNRs.

• the STL- and CTE-based lithographic procedures showed the best results with respect to edge roughness and crystallographic orientation control, however STL needs a conducting substrate and the transfer without damage of a GNR may be extremely challenging. CTE produces remarkably perfect zigzag edges, but the GNR widths achieved so far are not better than those produced by e-beam lithography.

In addition to moving-nanoparticle etching reaction, STL and CTE techniques reviewed in this paper, new top-down directions are currently explored, which may be more suitable for real applications. A recent example is a plasma-based etching process presenting high crystallographic selectivity brought about by hydrogenation of the edge carbon atoms of graphene.[31]

The bottom-up methods originating on one hand from the epitaxial growth on special facets of SiC and from organic chemistry are very promising, but presently still in their infancy. From these two methods the epitaxial growth of GNRs on SiC seems to be at present closer to technical applicability; however it is questionable if it will be possible to decrease the width of the GNRs in the range of 2 to 3 nm, needed for room temperature operation. The results obtained so far by assembling organic precursors on the Au(111) face, or other metals, are very promising, but here also the transfer of the GNRs to an insulating substrate has to be solved in one way or another. An additional difficulty which has to be handled is that a GNR of 2–3 nm in width has to be placed with very high precision onto a contact and that contact has to be an ohmic contact if electronic applications are envisaged.

An approach that may seem somewhat fantastic presently, but would solve most of the drawbacks mentioned above, could be based on the directed growth of all graphene circuitry by the controlled self-assembly of carefully chosen organic molecules along similar principles as outlined in ref. 111. If feasible, such a nanoarchitecture may be grown with conveniently large "contact pads" through which its communication with the micro- and macro-world can be achieved.

Acknowledgements

The present work was supported in Hungary by OTKA grant K67793. LPB gratefully acknowledges the agreement between the FNRS and HAS that made possible the cooperation with PhL.

References

1 A. K. Geim, *Science*, 2009, **324**, 1530–1534.
2 K. S. Novoselov, A. K. Geim, S. V. Morozov, D. Jiang, Y. Zhang, S. V. Dubonos, I. V. Grigorieva and A. A. Firsov, *Science*, 2004, **306**, 666–669.
3 P. Wallace, *Phys. Rev.*, 1947, **71**, 622–634.
4 H.-P. Boehm, R. Setton and E. Stumpp, *Pure Appl. Chem.*, 1994, **66**, 1893–1901.
5 P. Blake, E. W. Hill, a. H. Castro Neto, K. S. Novoselov, D. Jiang, R. Yang, T. J. Booth and a. K. Geim, *Appl. Phys. Lett.*, 2007, **91**, 063124.
6 A. Nagashima, K. Nuka, H. Itoh, T. Ichinokawa, C. Oshima, S. Otani and Y. Ishizawa, *Solid State Commun.*, 1992, **83**, 581–585.
7 T. Aizawa, R. Souda, S. Otani, Y. Ishizawa and C. Oshima, *Phys. Rev. Lett.*, 1990, **64**, 768–771.
8 Y.-M. Lin, C. Dimitrakopoulos, K. a. Jenkins, D. B. Farmer, H.-Y. Chiu, A. Grill and P. Avouris, *Science*, 2010, **327**, 662.
9 H. Şahin, R. T. Senger and S. Ciraci, *J. Appl. Phys.*, 2010, **108**, 074301.
10 D. A. Areshkin and C. T. White, *Nano Lett.*, 2007, **7**, 3253–3259.
11 S.-L. Li, H. Miyazaki, A. Kumatani, A. Kanda and K. Tsukagoshi, *Nano Lett.*, 2010, **10**, 2357–2362.
12 F. Schwierz, *Nat. Nanotechnol.*, 2010, **5**, 487–496.
13 Y. Zhu, S. Murali, W. Cai, X. Li, J. W. Suk, J. R. Potts and R. S. Ruoff, *Adv. Mater.*, 2010, **22**, 3906–3924.
14 Y. Wang, Z. Li, J. Wang, J. Li and Y. Lin, *Trends Biotechnol.*, 2011, **29**, 205–212.
15 Y. Shao, J. Wang, H. Wu, J. Liu, I. A. Aksay and Y. Lin, *Electroanalysis*, 2010, **22**, 1027–1036.
16 S. Stankovich, D. A. Dikin, G. H. B. Dommett, K. M. Kohlhaas, E. J. Zimney, E. A. Stach, R. D. Piner, S. T. Nguyen and R. S. Ruoff, *Nature*, 2006, **442**, 282–286.
17 S. Garaj, W. Hubbard, A. Reina, J. Kong, D. Branton and J. A. Golovchenko, *Nature*, 2010, **467**, 190–193.

18 M. D. Stoller, S. Park, Y. Zhu, J. An and R. S. Ruoff, *Nano Lett.*, 2008, **8**, 3498–3502.
19 L. P. Biró and P. Lambin, *Carbon*, 2010, **48**, 2677–2689.
20 L. Tapasztó, G. Dobrik, P. Lambin and L. P. Biró, *Nat. Nanotechnol.*, 2008, **3**, 397–401.
21 P. Nemes-Incze, G. Magda, K. Kamarás and L. P. Biró, *Nano Res.*, 2010, **3**, 110–116.
22 T. Pedersen, C. Flindt, J. Pedersen, N. Mortensen, A.-P. Jauho and K. Pedersen, *Phys. Rev. Lett.*, 2008, **100**, 136804.
23 J. A. Fürst, J. G. Pedersen, C. Flindt, N. a. Mortensen, M. Brandbyge, T. G. Pedersen and A.-P. Jauho, *New J. Phys.*, 2009, **11**, 095020.
24 Y.-w. Son, M. L. Cohen and S. G. Louie, *Nature*, 2006, **444**, 347–349.
25 V. Barone, O. Hod and G. E. Scuseria, *Nano Lett.*, 2006, **6**, 2748–2754.
26 X. Jia, J. Campos-Delgado, M. Terrones, V. Meunier and M. S. Dresselhaus, *Nanoscale*, 2011, **3**, 86–95.
27 A. Cresti and S. Roche, *New J. Phys.*, 2009, **11**, 095004.
28 B. Özyilmaz, P. Jarillo-Herrero, D. Efetov and P. Kim, *Appl. Phys. Lett.*, 2007, **91**, 192107.
29 K. A. Ritter and J. W. Lyding, *Nat. Mater.*, 2009, **8**, 235–242.
30 B. Krauss, P. Nemes-Incze, V. Skakalova, L. P. Biro, K. V. Klitzing and J. H. Smet, *Nano Lett.*, 2010, **10**, 4544–4548.
31 R. Yang, L. Zhang, Y. Wang, Z. Shi, D. Shi, H. Gao, E. Wang and G. Zhang, *Adv. Mater.*, 2010, **22**, 4014–4019.
32 M. Terrones, A. R. Botello-Méndez, J. Campos-Delgado, F. López-Urías, Y. I. Vega-Cantú, F. J. Rodríguez-Macías, A. L. Elías, E. Muñoz-Sandoval, A. G. Cano-Márquez and J.-c. Charlier, *Nano Today*, 2010, **5**, 351–372.
33 S. Ihara, S. Itoh and J. I. Kitakami, *Phys. Rev. B: Condens. Matter*, 1993, **48**, 5643–5647.
34 B. I. Dunlap, *Phys. Rev. B: Condens. Matter*, 1994, **50**, 8134–8137.
35 L. P. Biró, G. Márk, A. Koós, J. B. Nagy and P. Lambin, *Phys. Rev. B: Condens. Matter*, 2002, **66**, 165405.
36 A. Castro Neto, F. Guinea, N. Peres, K. Novoselov and A. Geim, *Rev. Mod. Phys.*, 2009, **81**, 109–162.
37 C. L. Kane and E. J. Mele, *Phys. Rev. Lett.*, 1997, **78**, 1932–1935.
38 M. S. Fuhrer, C. N. Lau and A. H. MacDonald, *MRS Bull.*, 2011, **35**, 289–295.
39 S. Das Sarma, S. Adam, E. Hwang and E. Rossi, *Rev. Mod. Phys.*, 2011, **83**, 407–470.
40 K. S. Novoselov, A. K. Geim, S. V. Morozov, D. Jiang, M. I. Katsnelson, I. V. Grigorieva, S. V. Dubonos and A. A. Firsov, *Nature*, 2005, **438**, 197–200.
41 M. I. Katsnelson, K. S. Novoselov and a. K. Geim, *Nat. Phys.*, 2006, **2**, 620–625.
42 C. Péterfalvi, A. Pályi and J. Cserti, *Phys. Rev. B: Condens. Matter Mater. Phys.*, 2009, **80**, 075416.
43 K. Nakada, M. Fujita, G. Dresselhaus and M. S. Dresselhaus, *Phys. Rev. B: Condens. Matter*, 1996, **54**, 17954–17961.
44 J. Guo, D. Gunlycke and C. T. White, *Appl. Phys. Lett.*, 2008, **92**, 163109.
45 P. Koskinen, S. Malola and H. Häkkinen, *Phys. Rev. Lett.*, 2008, **101**, 115502.
46 D. Querlioz, Y. Apertet, A. Valentin, K. Huet, A. Bournel, S. Galdin-Retailleau and P. Dollfus, *Appl. Phys. Lett.*, 2008, **92**, 042108.
47 M. Han, B. Özyilmaz, Y. Zhang and P. Kim, *Phys. Rev. Lett.*, 2007, **98**, 206805.
48 J. Li, Z. Li, G. Zhou, Z. Liu, J. Wu, B.-l. Gu, J. Ihm and W. Duan, *Phys. Rev. B: Condens. Matter Mater. Phys.*, 2010, **82**, 115410.
49 C. Berger, Z. Song, X. Li, X. Wu, N. Brown, C. Naud, D. Mayou, T. Li, J. Hass, A. N. Marchenkov, E. H. Conrad, P. N. First and W. A. de Heer, *Science*, 2006, **312**, 1191–1196.
50 L. A. Ponomarenko, F. Schedin, M. I. Katsnelson, R. Yang, E. W. Hill, K. S. Novoselov and A. K. Geim, *Science*, 2008, **320**, 356–358.
51 Z. Chen, Y. Lin, M. Rooks and P. Avouris, *Phys. E.*, 2007, **40**, 228–232.
52 M. Kim, N. S. Safron, E. Han, M. S. Arnold and P. Gopalan, *Nano Lett.*, 2010, **10**, 1125–1131.
53 T. Miyazaki, K. Hayashi, K. Kobayashi, Y. Kuba, H. Ohyi, T. Obara, O. Mizuta, N. Murayama, N. Tanaka, Y. Kawamura and H. Uemoto, *J. Vac. Sci. Technol., B: Microelectron. Nanometer Struct.–Process., Meas., Phenom.*, 2008, **26**, 2611–2619.
54 C. Stampfer, J. Güttinger, S. Hellmüller, F. Molitor, K. Ensslin and T. Ihn, *Phys. Rev. Lett.*, 2009, **102**, 056403.
55 J. Martin, N. Akerman, G. Ulbricht, T. Lohmann, J. H. Smet, K. von Klitzing and A. Yacoby, *Nat. Phys.*, 2007, **4**, 144–148.
56 P. Gallagher, K. Todd and D. Goldhaber-Gordon, *Phys. Rev. B: Condens. Matter Mater. Phys.*, 2010, **81**, 115409.
57 T. Tsukamoto and T. Ogino, *J. Phys. Chem. C*, 2011, **115**, 8580–8585.
58 L. Ci, Z. Xu, L. Wang, W. Gao, F. Ding, K. F. Kelly, B. I. Yakobson and P. M. Ajayan, *Nano Res.*, 2008, **1**, 116–122.
59 L. C. Campos, V. R. Manfrinato, J. D. Sanchez-Yamagishi, J. Kong and P. Jarillo-Herrero, *Nano Lett.*, 2009, **9**, 2600–2604.
60 S. S. Datta, D. R. Strachan, S. M. Khamis and A. T. C. Johnson, *Nano Lett.*, 2008, **8**, 1912–1915.
61 S. Konishi, W. Sugimoto, Y. Murakami and Y. Takasu, *Carbon*, 2006, **44**, 2338–2340.
62 F. Schäffel, J. H. Warner, A. Bachmatiuk, B. Rellinghaus, B. Büchner, L. Schultz and M. H. Rümmeli, *Nano Res.*, 2009, **2**, 695–705.
63 N. Severin, S. Kirstein, I. M. Sokolov and J. P. Rabe, *Nano Lett.*, 2009, **9**, 457–461.
64 L. Gao, W. Ren, B. Liu, Z.-S. Wu, C. Jiang and H.-M. Cheng, *J. Am. Chem. Soc.*, 2009, **131**, 13934–13936.
65 G. Binnig, H. Rohrer, C. Gerber and E. Weibel, *Phys. Rev. Lett.*, 1982, **49**, 57–61.
66 J. Tersoff and D. Hamann, *Phys. Rev. B*, 1985, **31**, 805.
67 A. A. Tseng, A. Notargiacomo and T. P. Chen, *J. Vac. Sci. Technol., B*, 2005, **23**, 877.
68 R. L. McCarley, S. a. Hendricks and A. J. Bard, *J. Phys. Chem.*, 1992, **96**, 10089–10092.
69 Q. Ouyang, K. Ishida and K. Okada, *Appl. Surf. Sci.*, 2001, **169–170**, 644–648.
70 H. Hiura, *Appl. Surf. Sci.*, 2004, **222**, 374–381.
71 S. Kondo, M. Lutwyche and Y. Wada, *Appl. Surf. Sci.*, 1994, **75**, 39–44.
72 J. Park, K. B. Kim, J.-Y. Park, T. Choi and Y. Seo, *Nanotechnology*, 2011, **22**, 335304.
73 G. Dobrik, L. Tapasztó, P. Nemes-Incze, P. Lambin and L. P. Biró, *Phys. Status Solidi B*, 2010, **247**, 896–902.
74 D. S. Ginger, H. Zhang and C. A. Mirkin, *Angew. Chem., Int. Ed.*, 2004, **43**, 30–45.
75 G. Binnig, C. Quate and C. Gerber, *Phys. Rev. Lett.*, 1986, **56**, 930–933.
76 J. G. Park, C. Zhang, R. Liang and B. Wang, *Nanotechnology*, 2007, **18**, 405306.
77 L. Weng, L. Zhang, Y. P. Chen and L. P. Rokhinson, *Appl. Phys. Lett.*, 2008, **93**, 093107.
78 S. Masubuchi, M. Arai and T. Machida, *Nano Lett.*, 2011, DOI: 10.1021/nl201448q.
79 S. Masubuchi, M. Ono, K. Yoshida, K. Hirakawa and T. Machida, *Appl. Phys. Lett.*, 2009, **94**, 082107.
80 K. Kumar, S. Strauf and E. H. Yang, *Nanosci. Nanotechnol. Lett.*, 2010, **2**, 185–188.
81 G. Rius, N. Camara, P. Godignon, F. Pérez-Murano and N. Mestres, *J. Vac. Sci. Technol., B: Microelectron. Nanometer Struct.–Process., Meas., Phenom.*, 2009, **27**, 3149.
82 S. Neubeck, F. Freitag, R. Yang and K. S. Novoselov, *Phys. Status Solidi B*, 2010, **247**, 2904–2908.
83 S. Neubeck, L. A. Ponomarenko, F. Freitag, A. J. M. Giesbers, U. Zeitler, S. V. Morozov, P. Blake, A. K. Geim and K. S. Novoselov, *Small*, 2010, **6**, 1469–1473.
84 A. J. M. Giesbers, U. Zeitler, S. Neubeck, F. Freitag, K. S. Novoselov and J. C. Maana, *Solid State Commun.*, 2008, **147**, 366–369.
85 N. Kurra, G. Prakash, S. Basavaraja, T. S. Fisher, G. U. Kulkarni and R. G. Reifenberger, *Nanotechnology*, 2011, **22**, 245302.
86 R. K. Puddy, P. H. Scard, D. Tyndall, M. R. Connolly, C. G. Smith, G. A. C. Jones, A. Lombardo, A. C. Ferrari and M. R. Buitelaar, *Appl. Phys. Lett.*, 2011, **98**, 133120.
87 Y. He, H. Dong, T. Li, C. Wang, W. Shao, Y. Zhang, L. Jiang and W. Hu, *Appl. Phys. Lett.*, 2010, **97**, 133301.
88 G. Lu, X. Zhou, H. Li, Z. Yin, B. Li, L. Huang, F. Boey and H. Zhang, *Langmuir*, 2010, **26**, 6164–6166.

89 Z. Osváth, A. Darabont, P. Nemes-Incze, E. Horváth, Z. E. Horváth and L. P. Biró, *Carbon*, 2007, **45**, 3022–3026.
90 H. R. Byon and H. C. Choi, *Nat. Nanotechnol.*, 2007, **2**, 162–166.
91 R. Koc and S. V. Cattamanchi, *J. Mater. Sci.*, 1998, **33**, 2537–2549.
92 C. Casiraghi, A. Hartschuh, H. Qian, S. Piscanec, C. Georgi, A. Fasoli, K. S. Novoselov, D. M. Basko and A. C. Ferrari, *Nano Lett.*, 2009, **9**, 1433–1441.
93 P. Nemes-Incze, G. Magda, K. Kamarás and L. P. Biró, *Phys. Status Solidi C*, 2010, **7**, 1241–1245.
94 X. Jia, J. Campos-Delgado, M. Terrones, V. Meunier and M. S. Dresselhaus, *Nanoscale*, 2011, **3**, 86–95.
95 X. Wang and H. Dai, *Nat. Chem.*, 2010, **2**, 661–665.
96 L. Xie, L. Jiao and H. Dai, *J. Am. Chem. Soc.*, 2010, **132**, 14751–14753.
97 K. Suenaga and M. Koshino, *Nature*, 2010, **468**, 1088–1090.
98 Z. Liu, K. Suenaga, P. J. F. Harris and S. Iijima, *Phys. Rev. Lett.*, 2009, **102**, 015501.
99 P. L. Giunta and S. P. Kelty, *J. Chem. Phys.*, 2001, **114**, 1807–1812.
100 S. Neubeck, Y. M. You, Z. H. Ni, P. Blake, Z. X. Shen, A. K. Geim and K. S. Novoselov, *Appl. Phys. Lett.*, 2010, **97**, 053110.
101 C. Berger, Z. Song, T. Li, X. Li, A. Y. Ogbazghi, R. Feng, Z. Dai, A. N. Marchenkov, E. H. Conrad, P. N. First and W. A. de Heer, *J. Phys. Chem. B*, 2004, **108**, 19912–19916.
102 Y.-M. Lin, C. Dimitrakopoulos, K. a. Jenkins, D. B. Farmer, H.-Y. Chiu, A. Grill and P. Avouris, *Science*, 2010, **327**, 662.
103 M. Sprinkle, M. Ruan, Y. Hu, J. Hankinson, M. Rubio-Roy, B. Zhang, X. Wu, C. Berger and W. a. de Heer, *Nat. Nanotechnol.*, 2010, **5**, 727–731.
104 L. P. Biró, L. Hevesi and P. Lambin, *Nanopages*, 2010, **5**, 1–3.
105 P. Kovacic and A. Kyriakis, *J. Am. Chem. Soc.*, 1963, **85**, 454–458.
106 W. J. Bailey and C.-W. Liao, *J. Am. Chem. Soc.*, 1955, **77**, 992–993.
107 A. C. Simonsen and H.-G. Rubahn, *Nano Lett.*, 2002, **2**, 1379–1382.
108 R. Mondal, B. K. Shah and D. C. Neckers, *J. Am. Chem. Soc.*, 2006, **128**, 9612–9613.
109 K. N. Houk, P. S. Lee and M. Nendel, *J. Org. Chem.*, 2001, **66**, 5517–5521.
110 E. Zojer, J. Cornil, G. Leising and J. Brédas, *Phys. Rev. B: Condens. Matter*, 1999, **59**, 7957–7968.
111 J. Cai, P. Ruffieux, R. Jaafar, M. Bieri, T. Braun, S. Blankenburg, M. Muoth, A. P. Seitsonen, M. Saleh, X. Feng, K. Müllen and R. Fasel, *Nature*, 2010, **466**, 470–473.
112 J. Wu, W. Pisula and K. Müllen, *Chem. Rev.*, 2007, **107**, 718–747.
113 X. Wang, Y. Ouyang, X. Li, H. Wang, J. Guo and H. Dai, *Phys. Rev. Lett.*, 2008, **100**, 206803.
114 S. Park, J.-Y. Wang, B. Kim, J. Xu and T. P. Russell, *ACS Nano*, 2008, **2**, 766–772.
115 J. Bai, X. Zhong, S. Jiang, Y. Huang and X. Duan, *Nat. Nanotechnol.*, 2010, **5**, 190–194.
116 M. Kim, N. S. Safron, E. Han, M. S. Arnold and P. Gopalan, *Nano Lett.*, 2010, **10**, 1125–1131.
117 T. Pedersen, C. Flindt, J. Pedersen, N. Mortensen, A.-P. Jauho and K. Pedersen, *Phys. Rev. Lett.*, 2008, **100**, 136804.
118 J. A. Fürst, J. G. Pedersen, C. Flindt, N. a. Mortensen, M. Brandbyge, T. G. Pedersen and A.-P. Jauho, *New J. Phys.*, 2009, **11**, 095020.
119 J. Eroms and D. Weiss, *New J. Phys.*, 2009, **11**, 095021.
120 T. Pedersen, C. Flindt, J. Pedersen, A.-P. Jauho, N. Mortensen and K. Pedersen, *Phys. Rev. B: Condens. Matter Mater. Phys.*, 2008, **77**, 245431.
121 R. Petersen, T. G. Pedersen and A.-P. Jauho, *ACS Nano*, 2011, **5**, 523–529.
122 J. A. Fürst, J. G. Pedersen, C. Flindt, N. a. Mortensen, M. Brandbyge, T. G. Pedersen and A.-P. Jauho, *New J. Phys.*, 2009, **11**, 095020.
123 J. Eroms and D. Weiss, *New J. Phys.*, 2009, **11**, 095021.
124 O. V. Yazyev, *Rep. Prog. Phys.*, 2010, **73**, 056501.
125 J. Fernández-Rossier and J. Palacios, *Phys. Rev. Lett.*, 2007, **99**, 177204.
126 W. L. Wang, S. Meng and E. Kaxiras, *Nano Lett.*, 2008, **8**, 241–245.
127 D. Yu, E. M. Lupton, M. Liu, W. Liu and F. Liu, *Nano Res.*, 2008, **1**, 56–62.
128 Y.-T. Zhang, Q.-M. Li, Y.-C. Li, Y.-Y. Zhang and F. Zhai, *J. Phys.: Condens. Matter*, 2010, **22**, 315304.
129 L. A. Ponomarenko, F. Schedin, M. I. Katsnelson, R. Yang, E. W. Hill, K. S. Novoselov and A. K. Geim, *Science*, 2008, **320**, 356–358.
130 C. Stampfer, E. Schurtenberger, F. Molitor, J. Güttinger, T. Ihn and K. Ensslin, *Nano Lett.*, 2008, **8**, 2378–2383.
131 T. Ihn, J. Güttinger, F. Molitor, S. Schnez, E. Schurtenberger, A. Jacobsen, S. Hellmüller, T. Frey, S. Dröscher and C. Stampfer, *Mater. Today*, 2010, **13**, 44–50.
132 E. A. Dobisz, S. L. Brandow, R. Bass and J. Mitterender, *J. Vac. Sci. Technol., B*, 2000, **18**, 107–112.
133 Y. Lu, B. Goldsmith, D. R. Strachan, J. H. Lim, Z. Luo and A. T. C. Johnson, *Small*, 2010, **6**, 2748–2754.
134 D. Strachan, D. Johnston, B. Guiton, S. Datta, P. Davies, D. Bonnell and A. Johnson, *Phys. Rev. Lett.*, 2008, **100**, 056805.
135 A. Rycerz, J. Tworzydło and C. W. J. Beenakker, *Nat. Phys.*, 2007, **3**, 172–175.
136 N. Peres, A. Castro Neto and F. Guinea, *Phys. Rev. B: Condens. Matter Mater. Phys.*, 2006, **73**, 195411.
137 H. van Houten and C. Beenakker, *Phys. Today*, 1996, **49**, 22–27.
138 J. Garcia-Pomar, A. Cortijo and M. Nieto-Vesperinas, *Phys. Rev. Lett.*, 2008, **100**, 236801.
139 Z. Z. Zhang, K. Chang and K. S. Chan, *Appl. Phys. Lett.*, 2008, **93**, 062106.
140 A. Saffarzadeh and R. Farghadan, *Appl. Phys. Lett.*, 2011, **98**, 023106.
141 Z. Wang and F. Liu, *ACS Nano*, 2010, **4**, 2459–2465.